

# Energy and generalized cross-helicity cascades in strong imbalanced collisionless Alfvén wave turbulence

G. MILOSHEVICH,<sup>1</sup> T. PASSOT,<sup>1</sup> AND P.L. SULEM<sup>1</sup>

<sup>1</sup>*Université Côte d’Azur, CNRS, Observatoire de la Côte d’Azur  
Laboratoire J.L. Lagrange, Boulevard de l’Observatoire, CS 34229, 06304 Nice Cedex 4, France*

## ABSTRACT

A pair of nonlinear diffusion equations, semi-phenomenologically derived from a two-field gyrofluid model, is used to study the dynamics of strong Alfvén wave turbulence, from MHD to electron scales. Special attention is paid to the regime of imbalance between the energies of counter-propagating waves commonly observed in the solar wind (SW), especially in regions relatively close to the Sun. In the collisionless regime where dispersive effects arise at scales comparable to or larger than those where dissipation becomes effective, the imbalance produced by a given injection rate of generalized cross-helicity (GCH), which is an invariant, is much larger than in the corresponding collisional regime, described by usual (or reduced) magnetohydrodynamics. The combined effect of high imbalance and ion Landau damping induces a steep energy spectrum for the transverse magnetic field at sub-ion scales. This spectrum is consistent with observations in highly Alfvénic regions of the SW, such as trailing edges, but does not take the form of a transition range continued at smaller scales by a shallower spectrum. This suggests that the observed spectra displaying such a transition result from the superposition of contributions originating from various streams with different degrees of imbalance. Furthermore, when injected at small scales in an already fully developed turbulence, for example under the effect of magnetic reconnection, GCH can in some instances undergo an inverse cascade, corresponding to a progressive enhancement of the imbalance at large scales.

## 1. INTRODUCTION

An important contribution to the SW dynamics originates from nonlinear interactions between counter-propagating Alfvén waves. Outgoing waves are emitted at the Sun’s surface, as a consequence of mechanisms such as reconnection in the chromospheric magnetic network (see e.g. the recent review by [Marsch \(2018\)](#)) which leads to injection of Alfvénic waves at the base of the fast SW ([McIntosh 2012](#)). Ingoing waves are created by reflection on density gradients ([Chandran & Hollweg 2009](#); [Chandran & Perez 2019](#)) and by velocity shear ([Roberts et al. 1992](#); [Breech et al. 2008](#)), or result from parametric decay instability ([Vias & Goldstein 1991](#); [Zanna et al. 2001](#)). The energies carried by these counter-propagating waves are usually unequal ([Tu et al. 1989](#); [Lucek & Balogh 1998](#); [Wicks et al. 2013](#)), with a degree of “imbalance” depending of the type of wind ([Tu et al. 1990](#); [Bruno et al. 2014](#); [Bruno et al. 2017](#); [D’Amicis et al. 2019](#)) and also on the distance from the Sun ([Roberts et al. 1987](#); [Marsch & Tu 1990](#)). Accurate in situ observations are now available for the turbulent energy cascades of Alfvén waves (AWs) or, at the sub-ion scales, kinetic Alfvén waves (KAWs) (see e.g. [Kiyani et al. \(2015\)](#); [Goldstein et al. \(2015\)](#) for

reviews). A precise understanding of how imbalance affects these cascades is however required in order to predict how much turbulence can heat and accelerate the SW plasma ([Chandran et al. 2010](#); [Cranmer et al. 2015](#); [Mallet et al. 2019](#)). Imbalance can also affect cosmic ray scattering efficiency, although a MHD numerical study by [Beresnyak et al. \(2011\)](#) shows almost no effect at these scales.

While, several theoretical and numerical studies have been devoted to Alfvénic turbulence at the MHD scales (see [Chen \(2016\)](#) for review), turbulence models based on cascades of KAWs have only been developed for the balanced case ([Cranmer & van Ballegoijen 2003](#)), the imbalanced regime at sub-ion scales remaining largely unexplored. Due to the computational cost of 3D imbalanced kinetic simulations, one is led to develop asymptotic models, isolating the AW dynamics within a spectral range extending from the MHD scales (larger than ion Larmor radius,  $\rho_i$ ) to the sub-ion scales, assuming a proton-electron homogeneous plasma subject to a strong ambient magnetic field. Such a description is provided by a Hamiltonian two-field gyrofluid retaining ion finite Larmor radius (FLR) corrections, parallel magnetic fluctuations and electron inertia ([Passot et al. 2018](#)). It takes the form of two dynamical equations for

the electron-gyrocenter density and the parallel magnetic potential, from which the electrostatic potential and the parallel magnetic fluctuations are easily derived.

Numerical simulations of the two-field gyrofluid are in progress. Here we concentrate on a reduction of this model in the form of nonlinear diffusion equations in Fourier space for the spectra of the two conserved quantities, energy and GCH (Passot & Sulem 2019). Concentrating on the effect of imbalance at scales larger than the electron skin depth  $d_e$ , electron inertia (easily reintroduced phenomenologically at the level of the phase velocity), is neglected in most of the simulations, which all address the strong turbulence regime.

The model isolates AWs and involves drastic simplifications, leaving for future study the influence of effects such as inhomogeneities and wind expansion. In some of the simulations, we nevertheless retain Landau damping which was shown to affect the sub-ion inertial range of balanced AW turbulence (Passot & Sulem 2015; Sulem et al. 2016), but neglect ion cyclotron damping and heating of the medium, considered for example by Cranmer & van Ballegooijen (2003), in spite of their potential effect on the dynamics.

## 2. THE MODEL

Assuming strong locality of the interactions in Fourier space, it is possible (see Passot & Sulem (2019)) to arrive at a phenomenological set of equations describing the time evolution of the transverse spectra  $E(k_\perp, t)$  and  $E_C(k_\perp, t)$  of energy and GCH respectively. The latter quantities are related to the energy spectra  $E^\pm(k_\perp, t)$  of the counter-propagating waves by  $E(k_\perp, t) = E^+(k_\perp, t) + E^-(k_\perp, t)$  and  $E_C(k_\perp, t) = (E^+(k_\perp, t) - E^-(k_\perp, t))/v_{ph}(k_\perp)$ , where the Alfvén phase velocity  $v_{ph}$  is a function of  $k_\perp$ . For completeness, we present here a simple purely heuristic derivation of this model.

Because the nonlinear interaction of KAWs is dominated by three-wave interactions (Galtier & Meyrand 2015), we consider a diffusion model with quadratic nonlinearities, in a form that preserves the existence of absolute-equilibrium solutions

$$\frac{\partial}{\partial t} \frac{E^\pm(k_\perp)}{2} = \frac{\partial}{\partial k_\perp} \left[ D^\mp(E^+, E^-, k_\perp) \frac{\partial}{\partial k_\perp} \frac{E^\pm(k_\perp)}{k_\perp} \right] + X^\pm. \quad (1)$$

The first term in the rhs is formally similar to the one given by David & Galtier (2019), when the turbulence is balanced ( $E^+ = E^-$ ). We, however, also need corrective terms  $X^\pm$  because the energies of the forward and backward propagating waves are not conserved independently in the presence of dispersion. Due to energy conservation it is clear that  $X^+ = -X^-$ . The equation

for the GCH  $E_C = (E^+ - E^-)/v_{ph}$  then reads

$$\frac{\partial}{\partial t} \frac{E_C}{2} = \frac{2X^+}{v_{ph}} + \left( \frac{\partial}{\partial k_\perp} + \frac{1}{v_{ph}} \frac{\partial v_{ph}}{\partial k_\perp} \right) \times \left\{ \sum_{r=\pm 1} (-1)^{\frac{r-1}{2}} \frac{D^{(-r)}}{v_{ph}} \frac{\partial}{\partial k_\perp} \left( \frac{E^{(r)}}{k_\perp} \right) \right\}. \quad (2)$$

The invariance of the GCH, which implies that the rhs of (2) should be of a conservative form, allows us to find  $X^+$ , constrained so that only the first term in brackets survives. Furthermore, dimensional analysis of the terms involved in Eq. (1), allows us to estimate  $D^\mp \sim k_\perp^3 / \tau_{tr}^\mp$ . The case with Landau damping is treated in Appendix A. In its absence,

$$D^\mp(E^\mp, k_\perp) = C' \frac{k_\perp^3}{(\tau_{NL}^\pm)^2 / \tau_w^\mp} = C' \frac{k_\perp^6 v_{ph} E^\mp}{\tilde{k}_\parallel^\mp}, \quad (3)$$

where  $\tilde{k}_\parallel^\mp$  measures the inverse parallel correlation length of  $\pm$  eddies or wave packets of wavenumber  $k_\perp$  in the transverse dimension). Here, we used arguments from Passot and Sulem (2019) to fix the nonlinear time  $\tau_{NL}^\pm = (k_\perp^3 v_{ph}^2 E^\pm)^{-1/2}$  consistently with the imbalanced strong MHD turbulence (see Lithwick et al 2007) and also wrote  $\tau_w^\mp = \tilde{k}_\parallel^\mp v_{ph}$ . The parameter  $C'$  is here taken equal to 1 in order to concentrate on a turbulence with a relatively strong nonlinearity parameter. In fact, the value of  $C'$  affects the location of the transition to the exponential decay (Passot & Sulem 2015). This is because it changes the relative importance of nonlinear transfer versus Landau dissipation. Retaining only strongly local interactions, the model ignores coupling between co-propagating waves since they have nearly the same velocity and can hardly overtake one another and interact. Interactions between such waves with comparable but not quasi-equal wavenumbers were considered by Voitenko & Keyser (2016), although they were shown not to significantly affect the dynamics in the context of the present model (Passot & Sulem 2019).

Assuming that both waves undergo a strong cascade  $\tau_{NL}^\pm \sim \tau_w^\mp$  one concludes  $\tilde{k}_\parallel^\pm = (k_\perp^3 E^\pm)^{1/2}$ . However, it is expected that in the imbalanced case, the  $+$  wave (which by definition is more energetic) will undergo a weaker cascade as suggested in MHD by Chandran (2008). This effect can be modeled by changing the definition of the parallel wavenumber  $\tilde{k}_\parallel^-$  of the “ $-$ ” wave affected by the interactions with the “ $+$ ” wave. To accomplish this uniformly, the parameter  $\chi$  is introduced along with the following ansatz

$$\tilde{k}_\parallel^{(r)} = (k_\perp^3 E^{(r)})^{1/2} (E^+ / E^-)^{(1-r)\chi/4}. \quad (4)$$

This expression reproduces the different models found in the literature depending on the free exponent  $\chi$ . The

value  $\chi = 0$  corresponds to the model of [Lithwick et al. \(2007\)](#)<sup>1</sup> where both waves are in a strong turbulent regime and satisfy the critical balance condition. In contrast,  $\chi = 1$  reproduces the model of [Chandran \(2008\)](#), where the stronger wave undergoes a weak turbulence cascade. The value  $\chi = 1/4$  corresponds to the model of [Beresnyak & Lazarian \(2008\)](#). The simulations without Landau damping described below (except the purely MHD ones) are performed with  $\chi = 1$  (appropriate in situations of large imbalance), as in the presence of dispersion any other value leads to an unphysical instability at the dissipation scale, as predicted in [Passot & Sulem \(2019\)](#). The stability range is extended to  $0.5 \leq \chi \leq 1$  when Landau damping is retained.

Finally, the set of reduced equations are cast as

$$\frac{\partial E}{\partial t} \frac{\partial}{\partial k_{\perp}} = \frac{\partial}{\partial k_{\perp}} \left\{ k_{\perp}^6 V \sum_{r=\pm 1} \frac{E^{(-r)}}{\tilde{k}_{\parallel}^{(-r)}} \frac{\partial}{\partial k_{\perp}} \left( \frac{E^{(r)}}{k_{\perp}} \right) \right\} \quad (5)$$

$$\frac{\partial E_C}{\partial t} \frac{\partial}{\partial k_{\perp}} = \frac{\partial}{\partial k_{\perp}} \left\{ k_{\perp}^6 \sum_{r=\pm 1} \frac{(-1)^{\frac{r-1}{2}} V E^{(-r)}}{v_{ph} \tilde{k}_{\parallel}^{(-r)}} \frac{\partial}{\partial k_{\perp}} \left( \frac{E^{(r)}}{k_{\perp}} \right) \right\}. \quad (6)$$

The weak turbulence equations given in [Passot & Sulem \(2019\)](#) are recovered when  $k^{\pm}$  is taken constant.

In the absence of Landau damping  $V = v_{ph}$ . It is constant at wavenumbers small compared with the smallest of the inverse ion Larmor radius  $\rho_i^{-1} = (\sqrt{2\tau}\rho_s)^{-1}$  (where  $\tau = T_{0i}/T_{0e}$  is the ion to electron temperature ratio at equilibrium) and the inverse sonic Larmor radius  $\rho_s^{-1} = (\sqrt{m_i/T_{0e}}\Omega_i)^{-1}$  (where  $m_i$  is the ion mass and  $\Omega_i$  the ion gyrofrequency), used as wavenumber unit (with  $\Omega_i^{-1}$  taken as time unit). It grows linearly ( $v_{ph} \approx \alpha k_{\perp}$ ) at smaller scales down to  $d_e = (2/\beta_e)^{1/2} \delta \rho_s$  (with  $\delta^2$  denoting the electron to proton mass ratio), where saturation occurs due to electron inertia.

In the strong turbulence regime, electron inertia can be reintroduced in the expression of  $v_{ph}$  which is the only quantity sensitive to the other kinetic effects. We treat Landau damping (see Appendix A) by adding dissipative terms  $-\gamma E$  and  $-\gamma E_C$  in Eqs. (5)-(6) respectively, where  $\gamma(k_{\perp}, \tilde{k}_{\parallel})$  is the AW Landau dissipation rate (dominated by electrons) of transverse and parallel wavenumbers  $k_{\perp}$  and  $\tilde{k}_{\parallel} = \max(\tilde{k}_{\parallel}^+, \tilde{k}_{\parallel}^-)$ . It also affects (mostly through the ions) the transfer time ([Passot & Sulem 2015](#)) and thus modifies the function  $V$  entering Eqs. (5)-(6), which becomes  $V = v_{ph}^2 / (v_{ph} + \mu \sqrt{2\tau})$

<sup>1</sup> In [Lithwick et al. \(2007\)](#), a slightly different interpretation of the critical balance is used where instead of the wave period, the correlation time of the straining imposed by oppositely directed waves is considered. The associated correlation lengths differ from those of our model but the predicted spectra are the same.

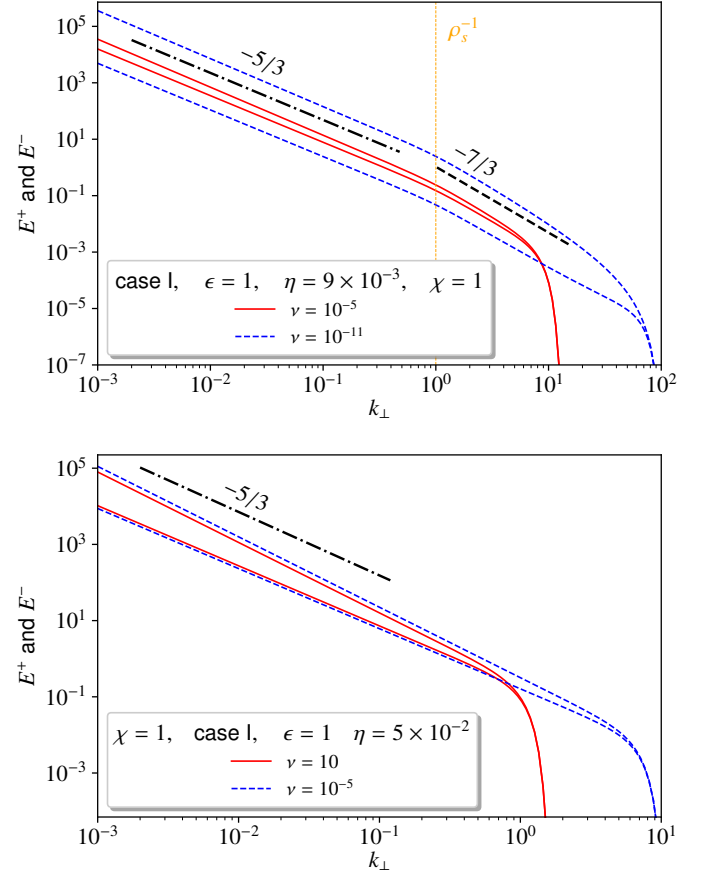


**Figure 1.** Changes in the imbalance between the  $E^{\pm}$  spectra when, for fixed injection rates, the dissipation scale is varied via different values of  $\nu$ . Top: fully dispersive equations. Bottom: pure MHD regime. Here and in similar further figures, the same color and line style are used for spectra  $E^+$  and  $E^-$  corresponding to the same run.

where  $\mu$  is a numerical constant (in the following,  $\mu = 3$ ).

Equations (5)-(6) were solved numerically using a finite difference scheme both in  $k_{\perp}$  (with a logarithmic discretization) and  $t$  (using a forward Euler scheme with adaptive time step), modifying a code developed for weak turbulence of gravitational waves ([Galtier et al. 2019](#)). We also introduced different grids for the fields and the fluxes, where fields are interpolated. Their coupling ensures better stability.

Simulations were performed for  $\beta_e = 2, \tau = 1$  (case I) typical of the SW at 1 AU, and  $\beta_e = 0.04, \tau = 10$  (case II), more suitable for regions closer to the Sun ([Roytershteyn et al. 2019](#)). For small  $\beta_e$ ,  $d_e$  significantly exceeds the electron Larmor radius  $\rho_e = \sqrt{2} \delta \rho_s$ , thus permitting to keep electron inertia while neglecting electron FLR corrections. Simulations with and without Landau

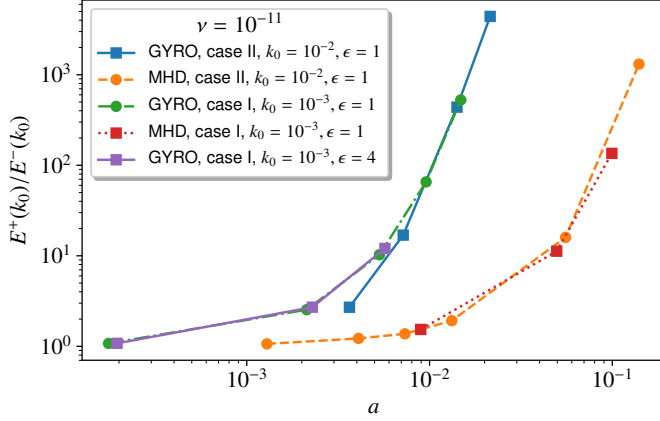


**Figure 2.** Imbalance at the outer scale  $k_0$  versus  $a = \sqrt{2/\beta_e \eta}/\epsilon$  (MHD) and  $a = \alpha \eta/\epsilon$  (GYRO).

damping were performed, the latter regime being of interest for comparison with analytical predictions. In this case, hyperdiffusive terms of the form  $\nu k_\perp^8 E(k_\perp, t)$  and  $\nu k_\perp^8 E_C(k_\perp, t)$ , are supplemented in Eqs. (5)-(6), with a coefficient  $\nu$  depending of the resolution and the parameters. The system is driven at large scale (injection wavenumber  $k_i$  in the range  $10^{-3}$  to  $10^{-2}$ ), dissipation taking place at small scales (dissipation wavenumber  $k_d$  between  $10^1$  and  $10^4$ ). Driving is performed either through boundary conditions by prescribing the values of the spectra  $E^\pm$  or of the fluxes  $\eta$  and  $\epsilon$  of energy and GCH at the smallest wavenumber  $k_0$ , or through injection terms of the form  $\varepsilon f(k_\perp)$  and  $\eta f(k_\perp)$  supplemented in the r.h.s. of Eqs. (5)-(6),  $f$  denoting a function with a support located near the injection wavenumber  $k_i$  such that  $\int_0^\infty f(k_\perp) dk_\perp = 1$ . Initial conditions consist of a spectral bump in the MHD range near the smallest retained wavenumber.

### 3. IMBALANCED TURBULENCE SPECTRA

When, in the absence of Landau damping, Eqs. (5)-(6) are integrated in the strong turbulence regime with prescribed boundary values  $E^\pm(k_0)$  and  $k_\perp^8$  dissipation terms, we observe a direct transfer of energy and GCH, with the development of power law spectra which progressively extend to the small scales, up to the moment when the dissipation scale is reached. Although the MHD-range spectrum that forms during this transient is very close to the  $k_\perp^{-5/3}$  stationary solution, the sub-ion spectra first develop a balanced regime (as a result of a faster transfer of energy than of GCH) with a spectrum steeper than  $k_\perp^{-8/3}$  before converging, while imbalance develops, towards an approximately  $-7/3$  steady state when imbalance is weak (not shown). Nonlinear diffusion models for finite-capacity systems (no ultra-violet

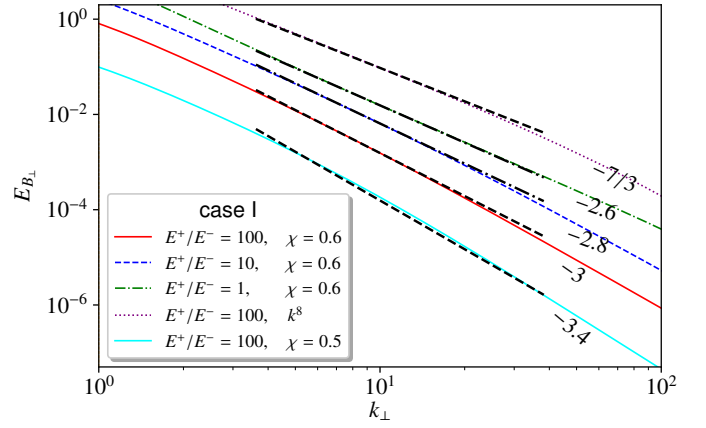
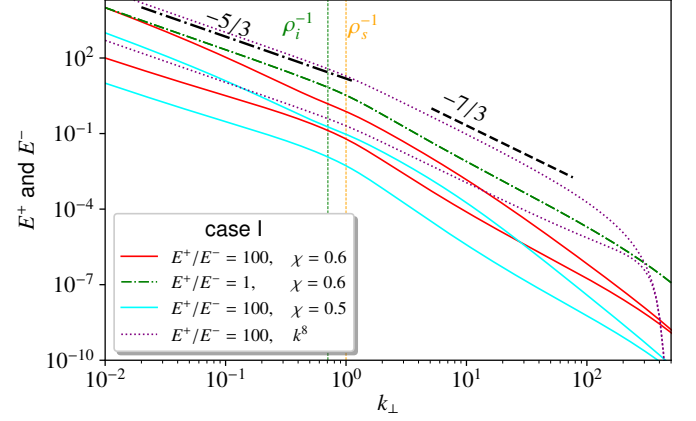


**Figure 3.** Top: spectra  $E^\pm$  when prescribed at the outer wavenumber  $k_0 = 10^{-2}$ , for four simulations ( $\delta = 0$ ): Landau damping is used in all simulations except when labeled by  $k^8$ . Bottom: Sub-ion  $E_{B_\perp}$  spectrum. Curves are shifted vertically for better readability.

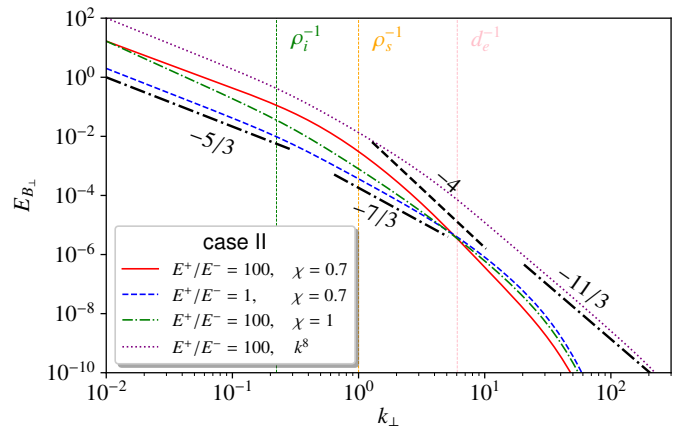


**Figure 4.**  $E_{B_\perp}$  spectrum ( $\delta^2 = 1/1836$ ). As imbalance is increased, spectra get steeper in the presence of Landau damping than with  $k^8$ -hyperdiffusion.



divergence of the energy) often exhibit such transient anomalous power-law spectra (Thalabard et al. 2015). The case of weak KAW turbulence has recently been addressed by David & Galtier (2019).

When the boundary conditions in  $k_0$  consist of prescribing energy  $\epsilon$  and GCH  $\eta$  fluxes, the imbalance between  $E^+$  and  $E^-$  at large scales is found to strongly depend on the small-scale extension of the dispersive range. This can be seen on Fig. 1 (top) to be compared with Fig. 1 (bottom) where the phase velocity is assumed constant (non-dispersive MHD). In both panels, the spectra are plotted at times at which a stationary regime with constant (positive) energy and GCH fluxes have established. In these simulations (case I with  $\delta = 0$ ), we varied the dissipation wavenumber by changing the hyperdiffusivity coefficient. In the MHD regime,  $E^\pm$  behave as power laws until the pinning scale (comparable to the dissipation scale) is approached. Differently, in the dispersive case, the spectra approach each other exponentially (consistent with the linear variation of  $\phi(k_\perp) = (1/2) \ln(E^+(k_\perp)/E^-(k_\perp))$  when  $\alpha\eta/\epsilon \ll 1$  (see Appendix C)). It follows that, in contrast with usual hydrodynamic turbulence, large-scale quantities depend on the dissipation scale  $k_d^{-1}$ . This effect is much stronger in the presence of dispersion where  $E^+(k_0)/E^-(k_0)$  varies exponentially with  $k_d$ , while it scales like a power law in MHD (see Eqs. (C.5) and (C.9)). In the dispersive case, the  $E_C$  spectrum steepens at  $k = 1$ , which is expected from the general relation (7.9) of Passot & Sulem (2019). The equation for the GCH spectrum being linear in  $E_C$ , the dissipative scales for  $E$  and  $E_C$  are the same. Since the GCH transfer is much slower than that of energy, this implies that, unless  $E_C$  increases at large scales (as it does), the rate of GCH dissipation  $\nu \int k_\perp^8 E_C dk_\perp$  cannot match the injected GCH or  $\eta$ . Consequently, the imbalance at large scales must increase.

Difference between the dispersive (GYRO) and non-dispersive (MHD) cases is also seen on Fig. 2 displaying the imbalance  $E^+(k_0)/E^-(k_0)$  at the outer wavenumber  $k_0$  (located in the MHD range) versus the parameter  $a \equiv v_{ph}(k_0)\eta/\epsilon \approx \sqrt{2/\beta_e}\eta/\epsilon$  (MHD), or  $a \equiv \alpha\eta/\epsilon$  (GYRO), in cases I and II. Graphs corresponding to different  $\beta_e$  collapse on the same curve, with an almost perfect agreement in MHD (in the GYRO simulations, the assumption  $v_{ph} = \alpha k_\perp$  is only approximate, especially close to the ion scale). Furthermore, changing  $\epsilon$  without changing the ratio  $\eta/\epsilon$  has no effect.

Influence of the degree of imbalance in the presence of Landau damping is considered in Fig. 3 in case I with  $\delta = 0$ , where, for comparison, a simulation involving hyperdiffusion is also presented. Top panel displays the

energy spectra  $E^\pm$ , while bottom panel shows the transverse magnetic spectrum  $E_{B_\perp}$  (see Appendix B). With hyperdiffusion, the  $k_\perp^{-5/3}$  MHD spectrum is continued at sub-ion scales by the classical  $k_\perp^{-7/3}$  range, the degree of imbalance significantly decreasing only near the pinning wavenumber. When Landau damping is retained, the degree of imbalance decreases with the scale, the more so when  $\chi$  is closer to 1 (visible in the top panel when comparing the runs with  $E^+(k_0)/E^-(k_0) = 100$  for  $\chi = 0.6$  and  $0.5$ ). In the sub-ion range, the steepening of  $E_{B_\perp}$  displayed in the bottom panel increases with the degree of imbalance (a more pronounced effect when  $\chi$  is smaller). Such a steepening is often observed as a transition range in the SW at 1AU, depending on the fluctuation power (Bruno et al. 2014), and sometimes associated with proton Landau damping (Sahraoui et al. 2010) and imbalance degree or Alfvénicity (Bruno et al. 2014; Bruno et al. 2017; D’Amicis et al. 2019). The present model suggests that both effects are to act simultaneously. An alternative mechanism for steepening of the spectrum related to reconnection is suggested by Vech et al. (2018).

Figure 4 displays  $E_{B_\perp}$  in case II with  $\delta^2 = 1/1836$ . For this relatively small  $\beta_e$ , an even stronger spectral steepening is observed for large imbalance. Furthermore, the multiplicative factor in front of  $E(k_\perp)$  in the estimate of  $E_{B_\perp}(k_\perp)$  is responsible for a steepening of the latter at scales smaller than  $d_e$ , visible in particular in the simulation with hyper-diffusivity,  $\chi = 1$ , and  $E^+(k_0)/E^-(k_0) = 100$ . A  $k_\perp^{-11/3}$  spectrum, classical for balanced IKAW turbulence (Chen & Boldyrev 2017; Passot et al. 2018; Roytershteyn et al. 2019) is still observed for this level of imbalance. Spectra, obtained with Landau damping and electron inertia, are also displayed in this figure: for  $\chi = 0.6$  with  $E^+(k_0)/E^-(k_0) = 1$  or  $E^+(k_0)/E^-(k_0) = 100$ , showing that the spectra get steeper as the imbalance increases, and for  $\chi = 1$  with  $E^+(k_0)/E^-(k_0) = 100$ , showing that the steepening is more pronounced as  $\chi$  is decreased. Such a steepening (although more moderate) is also observed in 3D fully-kinetic simulations (Grošelj et al. 2018).

#### 4. GCH INVERSE CASCADE

When turbulence develops from driving at intermediate scales a zero initial state, energy cascades to small scales. Since almost no energy is present at larger scales, a GCH cascade (associated with a transfer of energy between counter-propagating waves), cannot develop towards the large scales. A richer dynamics is possible

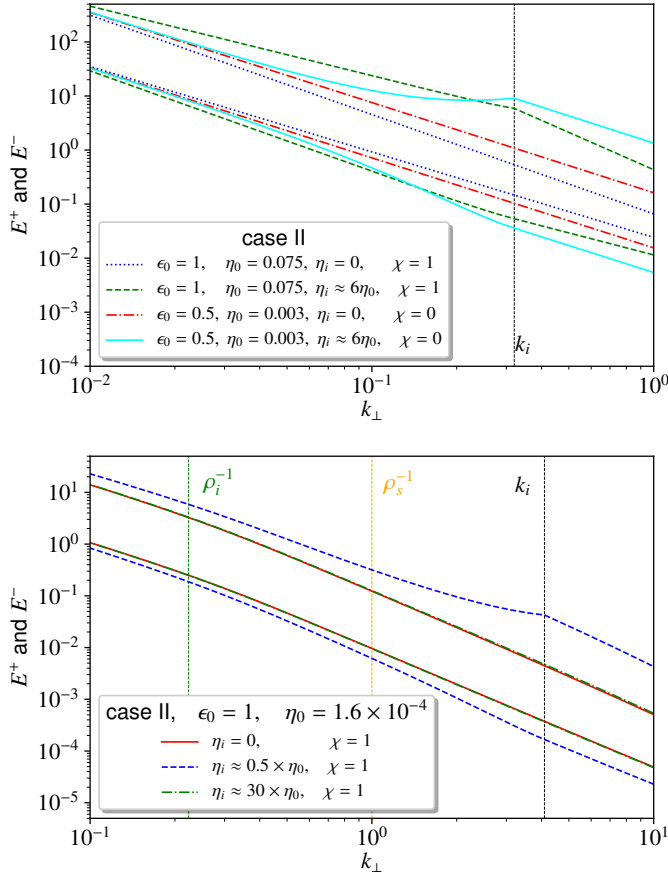


**Figure 5.**  $E^\pm$  spectra in MHD (top) and GYRO (bottom) simulations when GCH is injected at  $k_i \gg k_0$  with a rate  $\eta_i$ , in a developed turbulence without Landau damping driven at  $k_0$  with rates  $\epsilon_0$  and  $\eta_0$ .

when GCH injection is supplemented to an already developed turbulence. Note that absolute equilibrium arguments (Passot et al. 2018) cannot easily discriminate between the two situations.

In the following, the  $E^\pm$  spectra are prescribed at the outer wavenumber  $k_0$ . After a stationary state is reached, injection of  $E^+$  energy is made at a wavenumber  $k_i$ . In some instances, an inverse cascade of GCH develops, corresponding to a progressive enhancement of the imbalance towards the large scales. We infer the inverse cascade from the observation of stationary flat negative flux of GCH at wavenumbers smaller than the injection scale. To our knowledge this effect has not been reported earlier. In the presence of ambient magnetic-field and density gradients, a situation more suited to the solar corona, an inverse cascade of energy of the dominant wave was found by van Ballegooijen et al. (2017) using reduced MHD.

Let us first address the case where the driving takes place in the MHD range in a situation where the imbalance is strong, leading to assumption  $\chi = 1$ . In the initial steady state, the level of imbalance at the outer wavenumber  $k_0$  is related to the fluxes of energy  $\epsilon_0$  and of GCH  $\eta_0$  and to the pinning wavenumber  $k_d$  by  $\frac{E^+(k_0)}{E^-(k_0)} = \left(\frac{k_d}{k_0}\right)^{\frac{16a_0}{3-2a_0}}$ , where  $a_0 = \eta_0(2/\beta_e)^{1/2}/\epsilon_0$  (see Eq. (C.5, left)). We then inject GCH at  $k_i$  with a rate  $\eta_i$ . When  $\eta_i$  is greater than a critical value  $\eta_c$ , an inverse GCH cascade develops, as seen in Fig. 5 (top). At criticality, the GCH flux for wavenumbers smaller than  $k_i$  is zero. It follows from Eq. (C.5, right), that  $\phi$  is constant in that range so that  $E^+(k_i)/E^-(k_i) = E^+(k_0)/E^-(k_0)$  (i.e. the  $E^+$  and  $E^-$  spectra are parallel). Since  $\eta = 0$  for  $k < k_i$ , one gets that  $\eta = \eta_c$  for  $k > k_i$ . Applying again Eq. (C.5, left) between  $k_i$  and  $k_d$  leads to  $\frac{E^+(k_i)}{E^-(k_i)} = \left(\frac{k_d}{k_i}\right)^{\frac{16a_c}{3-2a_c}}$ , with  $a_c = (2/\beta_e)^{1/2}\eta_c/\epsilon_i$ , where  $\epsilon_i$  is the energy flux that establishes for  $k > k_i$ . We thus get

$$\frac{a_c(3-2a_0)}{a_0(3-2a_c)} = \frac{\ln k_d/k_0}{\ln k_d/k_i}. \quad (7)$$

When both  $a_0$  and  $a_c$  are assumed small compared to unity,  $\epsilon$  can be taken constant throughout the whole wavenumber range (as observed in the simulations) and the l.h.s. of Eq. (7) reduces to  $\eta_c/\eta_0$ . Numerical simulations were performed with different values of  $k_i$  showing that the ratio  $\eta_c/\eta_0$  indeed displays a slow increase with  $k_i$ , compatible with a logarithmic dependence (not shown).

When the level of imbalance is smaller we choose  $\chi = 0$ , to make the analysis simpler. We proceed as above, and using Appendix C.2, find that, for  $k_\perp < k_i$ , if  $\phi \neq \psi$ , the difference  $\phi - \psi$  asymptotically approaches zero when  $k_\perp$  decreases. This corresponds to the absence of an inverse cascade. This point is illustrated in Fig. 5 (top) which displays an increase of imbalance at small scales but not at large scales, in contrast with the case  $\chi = 1$ .

When injection takes place in the dispersive range (with  $\chi = 1$ ), assuming  $\alpha\eta/\epsilon$  is small,  $\phi$  is approximately constant and thus the level of imbalance  $E^+(k_0)/E^-(k_0)$  depends on  $k_d$  and  $\alpha\eta/\epsilon$ , but not on  $k_0$  (see Eq. (C.9)). In other words, the level of imbalance is mostly sensitive to the pinning scale. The transition to inverse cascade is again determined by imposing  $\eta = 0$  for  $k_\perp < k_i$ . Since  $k_d$  is not significantly affected by the injection at  $k_i$ ,  $\eta_c \approx \eta_0$ , whatever the value of  $k_i$ . Figure 5 (bottom) illustrates the development of a GCH inverse cascade for  $k_\perp < k_i$ , as can be seen by an enhanced imbalance at large scales compared with the initial state (given by  $\eta_i = 0$ ). Interestingly, when  $\eta_i \gg \eta_c$ , a significant fraction of the injected GCH is also transferred to

smaller scales. Note that since the degree of imbalance increases exponentially with the GCH injection rate, an injection rate much smaller than in the non-dispersive regime is sufficient to induce an inverse cascade compared to the non-dispersive regime. In the SW, dispersive scales are always present, making the possibility of an inverse cascade relevant. It would be of interest to investigate whether the process by which reconnection events can generate an inverse flux toward larger scales (Franci et al. 2017) can also generate imbalance in the case where counter-propagating KAWs are unequally generated at the reconnection site. The present modeling could also be useful to analyze the recently predicted cascade reversal at  $d_e$  in a reduced two-fluid model (Miloshevich et al. 2018) and a 3D extended magnetohydrodynamic model (Miloshevich et al. 2017).

## 5. CONCLUSION

This letter provides an analysis of the influence of imbalance between the energies of counter-propagating AWs, on the cascades developing in a collisionless plasma. It is aimed to contribute to the understanding of regimes encountered in the SW, particularly in regions close to the Sun explored by space missions such as Parker Solar Probe or Solar Orbiter.

The main results of the model simulations can be summarized as follows. (i) The imbalance produced by large-scale injection of GCH at a prescribed rate is enhanced

by wave dispersion. (ii) A steep range in the spectrum of the transverse magnetic fluctuations, consistent with the transition region reported in SW observations (Sahraoui et al. 2010), develops at the ion scales, under the combined influence of Landau damping and strong imbalance, an effect enhanced when  $\beta_e$  is decreased. We conjecture that the simulation results can be more specifically related to the observations inside the trailing edge, which is characterized by the highest level of Alfvénicity, i.e. imbalance (Bruno et al. 2014). Existence of a shallower spectrum at smaller scales is then expected to originate from SW regions that are less imbalanced and more energetic at these scales. (iii) Under some conditions the system develops an inverse cascade of GCH when injected at small scales in an already fully developed turbulence.

Future works include the study of the parent two-field gyrofluid models which is in particular expected to address the question of the characteristic nonlinear time scale in imbalanced turbulence, evaluate the assumption of strongly local interactions and investigate the role of KAW decay instability. The influence on the global dynamics of the coupling of the AWs with the slow modes, important at small  $\beta_e$  as they can generate large-scale parametric decay instabilities, will be studied using an extension of the present gyrofluid including both kinds of waves.

## APPENDIX

### A. MODELING LANDAU DAMPING

The dissipation rate  $\gamma(k_\perp, k_\parallel)$  is evaluated from Eq. (D.21) of Howes et al. (2006), obtained from the linearized gyrokinetic equations in the limit  $\delta^2\tau \ll \beta_i = \tau\beta_e \ll 1$  (c.f. definitions in the text). In a non-dimensional form, one has

$$\gamma = \sqrt{\frac{\pi}{2}} \frac{1}{\beta_e} \left( \frac{\Gamma_0(\tau k_\perp^2)}{\tau^{3/2}} \exp \left[ -\frac{\bar{\omega}^2}{\tau\beta_e} \right] + \delta \right) k_\parallel k_\perp^2. \quad (\text{A1})$$

Here  $\bar{\omega}^2 = k_\perp^2(1 + \tau - \Gamma_0(\tau k_\perp^2))/(1 - \Gamma_0(\tau k_\perp^2))$ , where  $\Gamma_n(x) = I_n(x)e^{-x}$  and  $I_n$  is the first type modified Bessel function of order  $n$ . While Eq. (A1) includes both ion and electron Landau damping, at small  $\beta_e$ , the primary contribution comes from electrons, so that Eq. (63) of Howes et al. (2006) can also be used. Landau damping also affects the transfer times  $\tau_{tr}^\pm$  of both counter-propagating waves, due to the temperature homogenization process along the magnetic field lines on the correlation length scale  $k_\parallel^{\pm-1}$ . The associate time scale  $v_{th} \tilde{k}_\parallel^\pm$ , which explicitly arises in Landau fluid closures (Hammett et al. 1992; Snyder et al. 1997; Sulem & Passot 2015), being proportional to the thermal velocity  $v_{th}$  of the particles, is very short for the electrons and cannot affect the dynamics. It is in contrast relevant in the case of the ions for which it is given in the present units by  $(\tau_H^\pm)^{-1} = \mu\sqrt{2\tau} \tilde{k}_\parallel^\pm$ , where  $\mu$  denotes a numerical constant of order unity. We are thus led to write

$$\tau_{tr}^\pm = \tau_{NL}^\pm \left( \frac{\tau_{NL}^\pm}{\tau_w^\pm} + \frac{\tau_{NL}^\pm}{\tau_H^\pm} \right), \quad (\text{A2})$$

which leads to

$$V = \frac{v_{ph}^2}{v_{ph} + \mu\sqrt{2\tau}}. \quad (\text{A3})$$

### B. TRANSVERSE MAGNETIC ENERGY SPECTRUM

The transverse magnetic energy spectrum  $E_{B\perp}$ , commonly measured in the SW, can be related, at least approximately, to the total energy spectrum. Writing  $\mathbf{k} = (k_\perp, \theta, k_\parallel)$  in cylindrical coordinates, the total energy can be expressed as  $\mathcal{E} = \int E(k_\perp) dk_\perp$ , with an energy spectrum given by  $E(k_\perp) = (1/2) \int (s^2 |k_\perp L_e \hat{A}_\parallel|^2 + |k_\perp L_e \Lambda \hat{\varphi}|^2) dk_\parallel k_\perp d\theta$ , equivalent to Eq. (2.36) of [Passot & Sulem \(2019\)](#). Here,  $\hat{\varphi}(\mathbf{k})$  and  $\hat{A}_\parallel(\mathbf{k})$  refer to the Fourier transforms of the electrostatic and parallel magnetic potentials respectively,  $L_e = (1 + 2\delta^2 k_\perp^2 / \beta_e)^{1/2}$  and  $\Lambda$  defined in Eq. (2.17) of [Passot & Sulem \(2019\)](#) is a function of  $k_\perp$  which tends to 1 as  $k_\perp \rightarrow 0$  and is proportional to  $1/k_\perp$  in the sub-ion range. The first term in the integral rewrites  $L_e^2 E_{B\perp}$ , where  $E_{B\perp} = (s^2/2) \int |\hat{B}_\perp(\mathbf{k})|^2 dk_\parallel k_\perp d\theta$  corresponds to the magnetic energy spectrum, and the second one reduces in the MHD regime to the kinetic energy spectrum. Their difference, referred to as the residual energy spectrum, is observed to remain small if initially zero in direct numerical simulations of the parent gyrofluid. In spite of the nonlinear interactions, the solution can indeed be viewed as a superposition of eigenmodes of both polarizations (which satisfy  $s^2 |k_\perp L_e \hat{A}_\parallel|^2 = |k_\perp L_e \Lambda \hat{\varphi}|^2$ ), and we are thus led to write  $E_{B\perp}(k_\perp) \approx (1/2) L_e^{-2} E(k_\perp)$ .

### C. IMBALANCED REGIME

In the non-dispersive case, it is possible to relate the flux ratio  $\eta/\epsilon$  to the imbalance  $E^+(k_0)/E^-(k_0)$  at the outer scale. This can be done by rewriting the spectra in the form

$$\frac{E(k_\perp)}{k_\perp} = \rho(k_\perp) \cosh \phi(k_\perp), \quad \frac{v_{ph}(k_\perp) E_C(k_\perp)}{k_\perp} = \rho(k_\perp) \sinh \phi(k_\perp). \quad (\text{C.1})$$

This leads to

$$E^\pm(k_\perp) = \frac{1}{2} k_\perp \rho(k_\perp) e^{\pm \phi(k_\perp)}. \quad (\text{C.2})$$

Two cases are to be distinguished, depending on the value of  $\chi$ .

#### C.1. The case $\chi = 1$

From Eq. (5) we see that, in the case  $\chi = 1$ , solutions with constant fluxes  $\eta$  and  $\epsilon$  obey

$$\frac{d}{dk_\perp} \rho^2(k_\perp) = -\frac{2\varepsilon \tilde{k}_\parallel^+(k_\perp)}{k_\perp^7 v_{ph}(k_\perp)}, \quad \rho^2(k_\perp) \frac{d}{dk_\perp} \phi(k_\perp) = -\frac{\eta \tilde{k}_\parallel^+(k_\perp)}{k_\perp^7}, \quad (\text{C.3})$$

where  $\tilde{k}_\parallel^+ = k_\perp^2 \sqrt{\rho/2} \exp(\phi/2)$ .

- In the MHD regime where  $v_{ph} = \sqrt{2/\beta_e}$ , it is easily shown that, defining  $a = \eta v_{ph}/\epsilon$ ,

$$\phi = \phi_0 + a \ln \rho / \rho_0. \quad (\text{C.4})$$

When substituted into Eq. (C.3, left), this leads to  $\rho = \left( (3-2a) e^{\phi_0/2} \epsilon \sqrt{\beta_e} / (16\rho_0^a) \right)^{2/(3-2a)} k_\perp^{-8/(3-2a)}$ , which, after some algebra, prescribes for the MHD regime

$$\frac{E^+(k_0)}{E^-(k_0)} = \left( \frac{k_d}{k_0} \right)^{\frac{16a}{3-2a}}, \quad \phi = \phi_0 - \frac{8a}{3-2a} \ln \frac{k_\perp}{k_0}, \quad (\text{C.5})$$

where  $k_d$  denotes the pinning wavenumber. This prediction excellently matches the numerical results presented in Fig. 2.

- In the far sub-ion range,  $v_{ph} \approx \alpha k_\perp$ , where  $\alpha = 2\sqrt{\frac{1+\tau}{\beta_e(2+(1+\tau)\beta_e)}}$ . The relationship between  $\rho$  and  $\phi$  derived from Eq. (C.3) reads in this case

$$\frac{\alpha\eta}{\epsilon} k_\perp \frac{d}{dk_\perp} \ln \rho = \frac{d\phi}{dk_\perp}. \quad (\text{C.6})$$



If we assume  $\eta\alpha/\epsilon \ll 1$ ,  $\phi$  can be approximated by a constant  $\phi_0$  in Eq. (C.3, left) which is then solved as

$$\rho = \left( \frac{3\epsilon e^{\phi_0/2} \sqrt{\beta}}{10\alpha\sqrt{2}} \right)^{2/3} k_{\perp}^{-10/3}. \quad (\text{C.7})$$

Equation (C.6) becomes

$$\phi = \phi_0 - \frac{10}{3} \frac{\alpha\eta}{\epsilon} k_{\perp}, \quad (\text{C.8})$$

which determines the pinning wavenumber  $k_d$  where  $\phi$  vanishes. From Eq. (C.2), it is clear that for small  $\alpha\eta/\epsilon$ ,  $\phi$  will be nearly constant up to the vicinity of  $k_d$  where the spectra  $E^{\pm}$  approach each other exponentially. Therefore, we can obtain a dispersive imbalance relation, whose behavior is very different from the MHD case, namely

$$\frac{E^+(k_0)}{E^-(k_0)} = \exp\left(\frac{20\eta\alpha k_d}{3\epsilon}\right), \quad \phi = \phi_0 - \frac{10\eta\alpha k_d}{3\epsilon} \quad \text{when } k_d \gg k_0. \quad (\text{C.9})$$

### C.2. The MHD regime with $\chi = 0$

After some algebra, it is easy shown that the equations for  $\rho$  and  $\phi$  read

$$\rho \frac{d}{dk_{\perp}} \left( \rho^{1/2}(k_{\perp}) \cosh\left(\frac{\phi(k_{\perp})}{2}\right) \right) = -\frac{\epsilon}{2^{3/2} k_{\perp}^5 v_{ph}(k_{\perp})}, \quad \rho \frac{d}{dk_{\perp}} \left( \rho^{1/2}(k_{\perp}) \sinh\left(\frac{\phi(k_{\perp})}{2}\right) \right) = -\frac{\eta}{2^{3/2} k_{\perp}^5}. \quad (\text{C.10})$$

From here, defining  $\tanh \psi/2 = \eta v_{ph}/\epsilon$ , we derive ( $A$  being a constant),

$$\sqrt{\rho} \sinh \frac{\phi - \psi}{2} = A, \quad \frac{d\phi}{dk} = \frac{\epsilon/v_{ph}}{2^{1/2} k^5 A^3 \cosh \psi/2} \sinh^4 \frac{\phi - \psi}{2}. \quad (\text{C.11})$$

Assuming  $\phi = \psi$ , which is an attractive solution, the imbalance becomes independent of  $k_{\perp}$ , in the form

$$\frac{E^+(k_{\perp})}{E^-(k_{\perp})} = \left( \frac{\epsilon + \eta v_{ph}}{\epsilon - \eta v_{ph}} \right)^2. \quad (\text{C.12})$$

## REFERENCES

- Beresnyak, A., & Lazarian, A. 2008, *Astrophys. J.*, 682, 1070  
 Beresnyak, A., Yan, H., & Lazarian, A. 2011, *Astrophys. J.*, 728, 60  
 Breech, B., Matthaeus, W. H., Minnie, J., et al. 2008, *J. Geophys. Res.: Space Phys.*, 113, A08105  
 Bruno, R., Telloni, D., DeIure, D., & Pietropaolo, E. 2017, *Month. Not. R. Astro. Soc.*, 472, 1052  
 Bruno, R., Trenchi, L., & Telloni, D. 2014, *Astrophys. J. Lett.*, 793, L15  
 Chandran, B. D. G. 2008, *Astrophys. J.*, 685, 646  
 Chandran, B. D. G., & Hollweg, J. V. 2009, *Astrophys. J.*, 707, 1659  
 Chandran, B. D. G., Li, B., Rogers, B. N., Quataert, E., & Germaschewski, K. 2010, *Astrophys. J.*, 720, 503  
 Chandran, B. D. G., & Perez, J. C. 2019, *J. Plasma Phys.*, 85, 905850409  
 Chen, C. H. K. 2016, *J. Plasma Phys.*, 82, 535820602  
 Chen, C. H. K., & Boldyrev, S. 2017, *Astrophys. J.*, 842, 122  
 Cranmer, S. R., Asgari-Targhi, M., Miralles, M. P., et al. 2015, *Phil. Trans. R. Soc. London*, A373, 20140148  
 Cranmer, S. R., & van Ballegooijen, A. A. 2003, *Astrophys. J.*, 594, 573  
 D’Amicis, R., Matteini, L., & Bruno, R. 2019, *Month. Not. R. Astro. Soc.*, 483, 4665  
 David, V., & Galtier, S. 2019, *Astrophys. J. Lett.*, 880, L10  
 Franci, L., Cerri, S. S., Califano, F., et al. 2017, *Astrophys. J. Lett.*, 850, L16  
 Galtier, S., & Meyrand, R. 2015, 81, 325810106  
 Galtier, S., Nazarenko, S. V., Buchlin, E., & Thalabard, S. 2019, *Physica D*, 390, 84  
 Goldstein, M. L., Wicks, R. T., Perri, S., & Sahraoui, F. 2015, *Phil. Trans. R. Soc. A*, 373, 20140147  
 Grošelj, D., Mallet, A., Loureiro, N. F., & Jenko, F. 2018, *Phys. Rev. Lett.*, 120, 105101  
 Hammett, G. W., Dorland, W., & Perkins, F. W. 1992, *Phys. Fluids B*, 4, 2052

- Howes, G. G., Cowley, S. C., Dorland, W., et al. 2006, *Astrophys. J.*, 651, 590
- Kiyani, K. H., Osman, K. T., & Chapman, S. C. 2015, *Phil. Trans. R. Soc. A*, 373, 20140155
- Lithwick, Y., Goldreich, P., & Sridhar, S. 2007, *Astrophys. J.*, 655, 269
- Lucek, E. A., & Balogh, A. 1998, *Astrophys. J.*, 507, 984
- Mallet, A., Klein, K. G., Chandran, B. D. G., et al. 2019, *J. Plasma Phys.*, 85, 175850302
- Marsch, E. 2018, *Ann. Geophys.*, 36, 1607
- Marsch, E., & Tu, C.-Y. 1990, *J. Geophys. Res.*, 95 (A6), 8211
- McIntosh, S. W. 2012, *Space Sci. Rev.*, 172, 69
- Miloshevich, G., Lingam, M., & Morrison, P. J. 2017, *New J. Phys.*, 19, 015007
- Miloshevich, G., Morrison, P. J., & Tassi, E. 2018, *Phys. Plasmas*, 25, 072303
- Passot, T., & Sulem, P. L. 2015, *Astrophys. J. Lett.*, 812, L37
- . 2019, *J. Plasma Phys*, 85, 905850301
- Passot, T., Sulem, P. L., & Tassi, E. 2018, *Phys. Plasmas*, 25, 042107
- Roberts, D. A., Goldstein, M. L., Klein, L. W., & Matthaeus, W. H. 1987, *J. Geophys. Res.: Space Physics*, 92, 12023
- Roberts, D. A., Goldstein, M. L., Matthaeus, W. H., & Ghosh, S. 1992, *J. Geophys. Res.: Space Phys.*, 97, 17115
- Roytershteyn, V., Boldyrev, S., Delzanno, G. L., et al. 2019, *Astrphys. J.*, 870, 103
- Sahraoui, F., Goldstein, M. L., Belmont, G., Canu, P., & Rezeau, L. 2010, *Phys. Rev. Lett.*, 105
- Snyder, P. B., Hammett, G. W., & Dorland, W. 1997, *Phys. Plasmas*, 4, 3974
- Sulem, P. L., & Passot, T. 2015, *J. Plasma Phys.*, 81, 325810103
- Sulem, P. L., Passot, T., Laveder, D., & Borgogno, D. 2016, *Astrophys. J.*, 818, 66
- Thalabard, S., Nazarenko, S., Galtier, S., & Medvedev, S. 2015, *J. Phys. A: Math. Theor.*, 48, 285501
- Tu, C. Y., March, E., & Rausenbauer, H. 1990, *Geophys. Res. Lett.*, 17, 283
- Tu, C.-Y., Marsch, E., & Thieme, K. M. 1989, *J. Geophys. Res.*, 94 (A9), 11739
- van Ballegooijen, A. A., Asgari-Targhi, M., & Voss, A. 2017, *Astrophys. J.*, 849, 46
- Vech, D., Mallet, A., Klein, K. G., & Kasper, J. C. 2018, *Astrophys J.*, L27
- Vias, A. F., & Goldstein, M. L. 1991, *J. Plasma Phys.*, 46, 129152
- Voitenko, Y., & Keyser, J. D. 2016, *Astrophys. J. Lett.*, 832, L20
- Wicks, R. T., Roberts, D. A., Mallet, A., et al. 2013, *Astrophys. J.*, 778, 177
- Zanna, L. D., Velli, M., & Londrillo, P. 2001, *Astro. Astrophys.*, 367, 705